Revision 1

Multi-stage magma evolution recorded by apatite and zircon of adakite-like rocks: A case study from the Shatanjiao intrusion, Tongling region, Eastern China

JINGYA CAO[1, 2], HUAN LI[2,*], XIAOYONG YANG[1,*], LANDRY SOH TAMEHE[2], RASOUL ESMAEILI[2]

1. *CAS Key laboratory of Crust-Mantle Materials and Environments, University of Science and Technology of China, Hefei 230026, China*

2. *Key Laboratory of Metallogenic Prediction of Nonferrous Metals and Geological Environment Monitoring, Ministry of Education, Central South University, Changsha 410083, China*

Corresponding authors: lihuan@csu.edu.cn (H. Li) and xyyang@ustc.edu.cn (X.Y. Yang).

Abstract: The Shatanjiao pluton, located at the eastern Tongling region (Eastern China), is of great research significance for the study of magma evolutionary process since this pluton is related to the regional Cu–Au mineralization. Zircon U–Pb dating on two granodiorite samples from this pluton yields ages of 141.9 ± 3.1 Ma (MSWD = 0.07) and 141.9 ± 3.3 Ma (MSWD = 0.03), respectively, which overlap the range of intense Late Jurassic to Early Cretaceous magmatism in the Tongling region. Based

on the Sr content of apatite from the Shatanjiao granodiorites, they are subdivided into high Sr apatite (apatite-I; 754–1242 ppm, mean = 1107 ppm) and low Sr apatite (apatite-II; 415–613 ppm, mean = 507 ppm). Both apatite-I and apatite-II are characterized by high Sr and Sr/Y ratios, and inconspicuous negative Eu anomalies, indicating that these granodiorites have a likely adakites affinity. Considering their low Rb contents (<0.05 ppm), in-situ Sr isotopes of these apatite grains show $^{87}Sr/^{86}Sr$ ratios of 0.70848–0.71494 and 0.70767–0.71585 for apatite-I and apatite-II, respectively, indicating that the $^{87}Sr/^{86}Sr$ ratios of both apatite groups can represent the Sr isotopic compositions of their host rocks. Moreover, the La/Sm and Sr/Th ratios of both apatite groups suggest that the studied granodiorites might be sourced from the partial melting of subducted ocean slab and overlying sediments. Based on their zircon trace element compositions, the calculated temperature and oxygen fugacity for the magma are characterized by high temperatures (mean T = 646 °C) and high oxygen fugacity (mean Ce^{4+}/Ce^{3+} ratios = 341). On the basis of MgO, FeO, SiO_2 and ΣREE contents of apatite, we further suggest that apatite-I and apatite-II might have crystallized at the early and late stages of magma evolution, respectively. Since apatite-I has much higher Eu/Eu* ratios (0.56–0.76) but lower $(La/Yb)_N$ ratios (7.85–28.6) than apatite-II of 0.39–0.58 and 95.9–132, respectively, it is indicated that plagioclase, garnet, hornblende and zircon might control the trace element composition of melt during the magma evolutionary history, which were recorded by the apatite. Therefore, apatite can be an ideal tracer to reflect the sequence of multi-stage magma evolution.

Keywords: Apatite; U–Pb dating; Adakite-like rocks; Magma evolution; Shatanjiao

1 INTRODUCTION

Adakites are intermediate to felsic rocks which are assumed to be formed by partial melting of young (less than 25 Ma) oceanic slabs in hot subduction zones (Defant and Drummond 1990). Adakites are characterized by distinctive geochemical signatures such as high Sr but low Y contents as well as high Sr/Y and La/Yb ratios (Defant and Drummond 1990; Martin 1999; Martin et al. 2005). Further studies suggest that some intraplate magmatic rocks can also exhibit the identical geochemical signatures to typical adakites (e.g., Defant and Drummond 1993; Erwan et al. 2002; Gao et al. 2007; Richards and Kerrich 2007; Wang et al. 2019). These magmatic rocks are commonly classified as adakite-like rocks and record geochemical evidence of melting, assimilation, storage and homogenization (MASH) and/or assimilation, fractional crystallization (AFC) processes during their genesis and evolution (Chiaradia 2009). The AFC and MASH processes in the shallow and deep magma chambers are important for the formation of the adakite-like rocks, since the geochemical signatures of these rocks are mainly controlled by the crystallization of specific minerals such as plagioclase, rutile, ilmenite and clinopyroxene (± amphibole) in shallow depth, and/or garnet and amphibole in deep reservoirs (Rollinson 1993; Macpherson et al. 2006; Richards and Kerrich 2007). Both AFC and MASH processes can be detectable from

the geochemical and isotopic characteristics of magmatic rocks. However, it should be emphasized that homogenization of magmas in shallow magma chambers has a potential to obscure the whole-rock geochemical compositions of magmatic rocks, and thus make them useless for distinguishing the magmatic evolutionary processes. On the other hand, accessory minerals can record valuable information regarding the geochemical characteristic of magma sources and/or magmatic conditions and evolutionary paths. Hence, these minerals are widely used for unraveling the hidden magmatic processes.

Zircon and apatite are important accessory minerals in granitic rocks, as well as in high Sr/Y rocks (adakites or adakite-like rocks). These minerals contain various elements with different geochemical behavior such as rare earth elements (REE), Ti, Mn, Sr, and Y which are sensitive to the physico-chemical conditions as well as the geochemical composition of magmas (e.g., Watson and Harrison 2005; Trail et al. 2012; Miles et al. 2014; Pan et al. 2016; Bruand et al. 2017; Nathwan et al. 2020). Sr is highly compatible in apatite, whereas Rb is incompatible, therefore, the $^{87}Sr/^{86}Sr$ isotopic ratio of apatite will not significantly influenced by the radioactive decay of the $^{87}Rb/^{86}Sr$. This suggests that the $^{87}Sr/^{86}Sr$ isotopic ratios of apatite can reflect the Sr isotopic composition of its host magmas (Tsuboi and Suzuki 2003; Tsuboi 2005). In addition, the apatite is also an ideal mineral to explore the formation of arc magmas as well as the magma evolutionary history, what can result in can result in explosive volcanism and the formation of economically valuable magmatic-hydrothermal ore deposits (Nathwani et al. 2019).

Taking into account the above features of such accessory minerals, we have performed a series of in-situ analyses on zircon and apatite from the Shatanjiao granodiorites, which are located in the Tongling region in eastern China (Fig. 1). We have further performed trace element and Sr isotopic analyses of apatite from the studied granitoids. The combination of our new geochronological, geochemical and isotopic data aims to constrain the age, nature, source of the Shatanjiao pluton in the Tongling region. Meanwhile, this study specifically provides a new insight on magma evolution process in this region from the perspective of apatite.

2 GEOLOGICAL SETTING

The Tongling region in Anhui Province is one of the seven major mining districts in the Middle–Lower Yangtze River Metallogenic Belt (MLYRB). It is situated at the suture zone between the Yangtze Craton and the North China Craton, bounded by the Yangxing–Changzhou Fault (YCF) and the Tancheng–Lujiang Fault (TLF) (Fig. 1). The basement rocks beneath the MLYRB are mainly composed of Kongling Late Archean to Paleoproterozoic metamorphic rocks (Chen et al. 2001). The Kongling complex is dominated by tonalite–trondjemite–granodiorite (TTG) gneisses with ages of 3.45–3.2 Ga (Guo et al. 2014; Wei et al. 2019) and 2.9–2.8 Ga (Gao et al. 1999, 2011; Zhang et al. 2006). These basement rocks are covered in ascending order by a series of Sinian (Neoproterozoic) to Triassic carbonates and clastic sediments (Chang et al. 1991).

The Tongling region is famous for its large scale Cu–Au mineralization, and hosts several major ore fields (Shizishan, Xinqiao, Fenghuangshan and Shatanjiao; Fig. 2). The stratigraphic sequences of this region comprise the Silurian sandstone,

Upper Devonian to Lower Middle Triassic sandstones and carbonates, Middle–Upper Middle Triassic carbonates, Upper Jurassic tuffs and rhyolites and Cretaceous conglomerates, shales and sandstones (Fig. 2). In this region, faults are generally trending in NE, NS and NW direction, and control the distribution of granitic plutons and Cu–Au deposits. Seventy-six granitic plutons intruded into Silurian–Triassic sedimentary rocks of the Tongling region (Pan and Dong 1999). These intrusions are mainly composed of granodiorite, quartz diorite and pyroxene diorite among which granodiorite and quartz diorite are closely related to the regional Cu–Au mineralization. Previous studies suggested that these granitic rocks and Cu–Au mineralization in the Tongling region were both formed between 147 and 130 Ma, indicating that the large scale Cu–Au mineralization is genetically related to the Late Jurassic–Early Cretaceous granitic magmatism (e.g., Yang et al. 2011; Zhong et al. 2014; Cao et al. 2017; Xie et al. 2017; Liu et al. 2018; Xiao et al. 2020).

Located at the eastern Tongling region, the Shatanjiao pluton occupies an area of 5.5 km^2 and is intruded into the surrounding carbonate rocks, resulting in the skarnization and Cu-Au mineralization (Fig. 3). This pluton is composed of granodiorite with zircon U–Pb age of 141.4 ± 1.1 Ma (Wu et al. 2011). These granodiorites have high SiO_2, Al_2O_3 and NaO_2 contents, suggesting a high-K calc-alkaline affinity (Wu et al. 2011).

3 SAMPLING AND ANALYTICAL TECHNIQUES

3.1 Sample collection and description

Two granodiorite samples were collected from the Shatanjiao pluton, including a medium- to coarse-grained granodiorite (sample STJ09) and a fine- to medium-grained granodiorite (sample STJ01). The sample locations are shown in Fig. 3. Zircon and

apatite grains were separated from the two rock samples. Zircon grains were used for U–Pb dating and trace element composition analyses, whereas apatite grains were employed for Sr isotopic and trace element composition analyses.

These granodiorite samples are light grey-white in color, and display a massive structure and porphyritic texture (Fig. 4a and 4c). The medium- to coarse-grained granodiorite contains plagioclase (~40%), K-feldspar (~25%), quartz (~20%), biotite (~10%) and hornblende (~5%), with minor zircon, apatite, sphene and magnetite (Fig. 4b). The fine- to medium-grained granodiorite is composed of plagioclase (~30%), K-feldspar (~30%), quartz (~25%), biotite (~10%) and hornblende (~5%), with zircon, apatite, sphene and magnetite as accessory phases (Fig. 4d).

3.2 Cathodoluminescence (CL) and backscattered electron (BSE) imaging

Zircon and apatite grains were separated by conventional magnetic and heavy liquid techniques and hand-picked using a binocular microscope. They were then mounted in epoxy resin blocks and polished to obtain flat surfaces. All zircon grains were subjected to CL imaging, whereas BSE imaging were taken for apatite grains. Both images were employed to better characterize the internal structures of individual zircon and apatite grains, respectively. The CL and BSE images were obtained using a scanning electron microscope (SEM) housed at the Key Laboratory of Crust–Mantle Materials and Environments, Chinese Academy of Sciences, University of Science and Technology of China (Hefei, China).

3.3 Zircon U–Pb dating and trace element analysis

In situ zircon U–Pb dating and trace element concentrations analyses were performed using a Geolas Pro laser-ablation system simultaneously coupled to a Neptune Plus multiple-collector ICP–MS and a 7700x quadrupole ICP–MS at the Key

Laboratory for the study of focused Magmatism and Giant Ore Deposits, Xi'an Center of Geological Survey, China Geological Survey. A stationary laser ablation spot with a beam diameter of 30 μm was used for all analyses. The ablated aerosol was carried by helium and then combined with argon in a mixing chamber before being introduced to the ICP-MS plasma. NIST610 and 91500 was used as the reference standards. GJ-1 was used as the monitor standard for U–Pb dating analyses. Analytical errors for individual samples are presented as 2σ in Table 1, whereas uncertainties in weighted mean ages are quoted at 2σ (95% confidence) in concordia diagrams. The measurement accuracy was better than 96% (2σ). Trace element concentrations and U–Pb isotopic compositions were calculated using the software of GLITTER 4.4.4. The common Pb correction was conducted using the method proposed by Andersen (2002). Weighted mean age calculations and concordia diagrams were generated with Isoplot 3.0 (Ludwig 2003).

3.4 *In-situ* LA–ICP–MS trace element analysis of apatite

Trace element analysis of apatite was conducted by LA–ICP–MS at the Wuhan Sample Solution Analytical Technology Co., Ltd. (Wuhan, China). Detailed operating conditions for the laser ablation system and the ICP-MS instrument and data reduction are the same as given in Zong et al. (2017). Laser sampling was performed using a GeolasPro laser ablation system consisting of a COMPexPro 102 ArF excimer laser (wave length of 193 nm and maximum energy of 200 mJ) and a MicroLas optical system. An Agilent 7700e ICP–MS instrument was used to acquire ion-signal intensities. Helium was used as a carrier gas, and argon was used as a make-up gas and mixed with the carrier gas via a T-connector before injection into the ICP. A “wire” signal smoothing device was included in this laser ablation system (Hu et al. 2015). The spot size and frequency of the laser were set to 32 μm and 5 Hz, respectively. Trace

This is the peer-reviewed, final accepted version for American Mineralogist, published by the Mineralogical Society of America.
The published version is subject to change. Cite as Authors (Year) Title. American Mineralogist, in press.
DOI: https://doi.org/10.2138/am-2021-7871. http://www.minsocam.org/

element compositions of minerals were calibrated against various reference materials (BHVO–2G, BCR–2G and BIR–1G) without using an internal standard (Liu et al. 2008). Each analysis incorporated a background acquisition of approximately 20–30 s followed by 50 s period of sample data acquisition. The measurement accuracy was better than 97% (1σ). An Excel-based software ICPMSDataCal was used to perform off-line selection and integration of background and analyzed signals, time-drift correction, and quantitative calibrations (Liu et al. 2008).

3.5 *In-situ* LA–MC–ICP–MS strontium isotopic analysis of apatite

Sr isotopic measurements of apatite were performed using a Neptune Plus MC–ICP–MS (Thermo Fisher Scientific, Bremen, Germany) in combination with a Geolas HD excimer ArF laser ablation system (Coherent, Göttingen, Germany) at the Wuhan Sample Solution Analytical Technology Co. Ltd. (Wuhan, China). The Neptune Plus was equipped with nine Faraday cups fitted with 1011 Ω resistors. The Faraday collector configuration of the mass system was composed of an array from L4 to H3 to monitor Kr, Rb, Er, Yb and Sr. A combination of a high-sensitivity X-skimmer cone and Jet-sample cone was employed. In the laser ablation system, helium was used as a carrier gas for the ablation cell. For single-spot laser ablation, the spot diameter ranged from 60 to 160 μm depending on the Sr signal intensity. The pulse frequency was from 8 to 15 Hz, and the laser fluence was held constant at ~10 J/cm^2. The data reduction for LA–MC–ICP–MS analysis was conducted using ICPMSDataCal (Liu et al. 2010). The interference correction strategy was the same as that reported by Tong et al. (2016). The regions of integration for both gas background and sample were initially selected, and no additional Kr peak stripping was applied following the background correction, which removed the background Kr+ signals. Then, interferences were corrected in the following sequence: (1) the interferences of $^{168}Er^{++}$ on ^{84}Sr, $^{170}Er^{++}$ and

208 $^{170}Yb^{++}$ on ^{85}Rb, $^{172}Yb^{++}$ on ^{86}Sr, and $^{174}Yb^{++}$ on ^{87}Sr were corrected based on the
209 measured signal intensities of $^{167}Er^{++}$, $1^{73}Yb^{++}$ and the natural isotope ratios of Er and
210 Yb (Berglund and Wieser 2011); and (2) the isobaric interference of ^{87}Rb on ^{87}Sr was
211 corrected by monitoring the ^{85}Rb signal intensity and a user-specified $^{87}Rb/^{85}Rb$ ratio
212 using an exponential law for mass bias. The user-specified $^{87}Rb/^{85}Rb$ ratio was
213 calculated by measuring some reference materials with a known $^{87}Sr/^{86}Sr$ ratio.
214 Following the interference corrections, mass fractionation of Sr isotopes was corrected
215 by assuming $^{88}Sr/^{86}Sr = 8.375209$ (Tong et al. 2016) and applying the exponential law.
216 Two natural apatite crystals (Durango and MAD) were used as unknown samples for
217 *in-situ* Sr isotopic analyses of apatite. The uncertainty of the $^{88}Sr/^{86}Sr$ ratio (2σ) for
218 single measurements was 0.0003–0.0004. The analyzed $^{88}Sr/^{86}Sr$ ratios of Durango and
219 MAD crystals in this study are 0.706346 ± 0.000516 and 0.711879 ± 0.000157,
220 respectively, which are within error of the reported ratios of 0.71180 and 0.70632,
221 respectively (Yang et al. 2014).

222 # 4 RESULTS

223 ## 4.1 Zircon U–Pb ages

224 LA–ICP–MS zircon U–Pb age data for two granodiorite samples from the
225 Shatanjiao pluton are presented in Table 1. Most zircon grains from the fine- to
226 medium-grained granodiorite (sample STJ01) are euhedral, and have lengths of
227 100–200 μm and aspect ratios of 1:1 to 3:1. These zircon grains display internal
228 oscillatory zoning, suggesting a magmatic origin (Hoskin and Schaltegger 2003; Fig.
229 5). Their Th and U contents are 69–303 ppm and 265–651 ppm, respectively, with
230 Th/U ratios of 0.25–0.54. Twenty-two analyses of magmatic domains give concordant
231 or nearly concordant $^{206}Pb/^{238}U$ ages ranging from 138 to 145 Ma (Table 1), yielding a

weighted average age of 141.9 ± 3.1 Ma (MSWD = 0.07; Figs. 6a–b). This age is interpreted as the crystallization age of the fine- to medium-grained granodiorite.

Zircon grains from the medium- to coarse-grained granodiorite (sample STJ09) are mostly euhedral or subhedral and have lengths of 150–200 μm and aspect ratios of 1:1–3:1. The CL imaging also shows internal oscillatory zoning, suggesting a magmatic origin for these zircon grains (Hoskin and Schaltegger 2003; Fig. 5). They have Th (75–305 ppm) and U contents (173–411ppm), with Th/U ratios of 0.41–0.85. Twenty-five analyses of magmatic domains yield concordant $^{206}Pb/^{238}U$ age group near or on the concordia curve (Fig. 6c). The $^{206}Pb/^{238}U$ ages of these zircon grains range from 139 to 145 Ma (Table 1), yielding a weighted average age of 141.9 ± 3.3 Ma (MSWD = 0.03; Fig. 6d). This age is further interpreted as the crystallization age of the medium- to coarse-grained granodiorite.

4.2 Zircon trace element compositions

The trace element concentrations of zircon grains are shown in Table 2. Zircon grains from the fine- to medium grained-granodiorite have Ti contents of 1.15–7.86 ppm and total rare earth element (ΣREE) of 205–853 ppm. They exhibit enrichment in heavy rare earth elements (HREE), depletion in light rare earth elements (LREE), and relatively low LREE/HREE ratios of 0.02–0.08. Their chondrite-normalized REE patterns are characterized by negative Eu anomalies (Eu/Eu* = 0.57–0.75, mean = 0.68) and positive Ce anomalies (Ce/Ce* = 69–605, mean = 266), which are similar features of zircon of magmatic origin (Fig. 7a; Hoskin and Schaltegger, 2003).

Zircon grains from medium- to coarse-grained granodiorite are also characterized by variable contents of Ti (1.73–5.36 ppm) and ΣREE (152–958 ppm). These zircon

255 grains further display enrichment in HREE, depletion in LREE and relatively low
256 LREE/HREE ratios of 0.02–0.05. Their chondrite-normalized REE patterns also show
257 relatively negative Eu anomalies (Eu/Eu* = 0.57–0.74, mean = 0.65) and positive Ce
258 anomalies (Ce/Ce* = 31–899, mean = 233), which indicate a magmatic origin for the
259 zircon grains of this sample (Fig. 7b; Hoskin and Schaltegger, 2003).

260 **4.3 Apatite major and trace element compositions**

261 The major and trace element compositions of apatite from the granodiorite
262 samples of the Shatanjiao pluton are given in Table 3. Apatite grains from the fine- to
263 medium-grained granodiorite (apatite-I) and from the medium- to coarse-grained
264 granodiorite (apatite-II) both mainly occur as euhedral or subhedral crystals with no
265 evidence of hydrothermal alteration under BSE images (Fig. 8), indicating that these
266 apatite grains have a magmatic origin. Apatite-I has P_2O_5, CaO, MgO, SiO_2, MnO, FeO
267 and Na_2O contents of 42.4–44.1 wt%, 55.0–56.7 wt%, 0.02 wt%, 0.22–0.55 wt%,
268 0.08–0.09 wt%, 0.06–0.07 wt%, and 0.03–0.08 wt%, respectively. Apatite-II has
269 similar contents of P_2O_5 (43.3–44.0 wt%) and CaO (54.9–55.7 wt%), but higher SiO_2
270 (0.34–0.48 wt%), lower MnO (0.04–0.48 wt%), FeO (0.03–0.06 wt%) and MgO
271 (0.01–0.02 wt%) contents than those of apatite-I (Fig. 9). However, apatite-I and
272 apatite-II both are featured by low MnO and SiO_2 contents, which further suggest a
273 magmatic origin (Fig. 10).

274 Apatite-I is characterized by high contents of Sr (754–1242 ppm) and Y (113–575
275 ppm), but low Th (1.50–7.53 ppm) and U (2.50–9.75 ppm) contents relative to
276 apatite-II showing Sr, Y, Th and U concentrations of 415–612 ppm, 109–194 ppm,
277 16.3–28.1 ppm and 5.27–12.2 ppm, respectively. Apatite-I and apatite-II both show
278 low Rb concentrations (mostly lower than 0.05 ppm). In terms of REE compositions,

apatite-I has low and variable ΣREE (668–2239 ppm) when compared to apatite-II (3145–4933 ppm). Both apatite-I and apatite-II are characterized by enrichment in LREE and depletion in HREE, with $(La/Yb)_N$ ratios of 7.85–28.6 and 95.9–132, respectively (Fig. 11). Apatite-I has higher negative Eu anomalies (Eu/Eu* = 0.56–0.76) than those of apatite-II (Eu/Eu* = 0.39–0.58). Apatite-I did not show obvious Ce anomalies, whereas apatite-II has slightly negative Ce anomalies (Ce/Ce* = 0.87–0.93).

4.4 Apatite Sr isotopes

The strontium isotopic compositions of apatite from the granodiorite samples of the Shatanjiao pluton are given in Table 4. The $^{87}Sr/^{86}Sr$ ratios of apatite-I and apatite-II vary between 0.70848–0.71494 and 0.70767–0.71585, respectively (Fig. 12). In addition, both apatite-I (sample STJ01) and apatite-II (sample STJ09) have relatively low $^{87}Rb/^{86}Sr$ ratios, ranging from 0.00032 to 0.01119 and from 0.00043 to 0.01822, respectively. This suggests that the ^{87}Sr produced by radioactive decay of ^{87}Rb could be ignored and the measured $^{87}Sr/^{86}Sr$ ratios of scheelite could be equal to their initial ratios at the time of crystallization or element redistribution of the studied granodiorites (Kozlik et al. 2016).

5 DISCUSSION

5.1 Age and adakite-like rock affinity

The granodiorite samples from the Shatanjiao pluton were dated at 141.9 ± 3.1 Ma (sample STJ01) and 141.9 ± 3.3 Ma (sample STJ09), which overlap the range (148–130 Ma) of intense Late Jurassic to Early Cretaceous intermediate-acid igneous magmatism in the Tongling region (Yang et al. 2011; Xie et al. 2017; Liu et al. 2018).

Compared with non-adakite-like rocks, high Sr, low Y and Yb, high Sr/Y ratios, and lack of negative Eu anomalies are typical geochemical features of adakite-like rocks (Defant and Drummond 1990; Martin 1999; Martin et al. 2005). Experimental study by Watson and Green (1981) has revealed that Sr and REE are highly compatible in apatite, therefore, the apatite might inherit high Sr and low Y contents, high Sr/Y ratios and inconspicuous Eu anomalies from the melt. In this study, both apatite-I and apatite-II show medium Eu anomalies (Eu/Eu* = 0.56–0.76 and 0.39–0.58, respectively) and high Sr/Y ratios (1.60–8.79 and 2.75–4.64, respectively), indicating that the studied granodiorites belong to the adakite-like rocks (Fig. 13; Pan et al. 2016). Our results are in good agreement with previous whole-rock geochemical studies of the Shatanjiao granodiorites by Wu et al. (2011). Overall, this indicates that the Sr/Y and Eu/Eu* ratios of apatite could be a valid tracer for identifying the adakite-like rocks.

5.2 Characteristics of magma source

Rb is highly incompatible in apatite due to the extremely low partition coefficient between apatite and granitic melt ($D_{Rb}^{apatite/melt}$ = 0.0013; Prowatke and Klemme 2006). In contrast, Sr is highly compatible in apatite since the Sr^{2+} can substitute Ca^{2+} into the lattice of apatite (Pan and Fleet 2002). It means that the $^{87}Sr/^{86}Sr$ ratios of apatite can be regarded as the initial $^{87}Sr/^{86}Sr$ ratios of their primary magma. In this study, the $^{87}Sr/^{86}Sr$ ratios of apatite-I (0.70848–0.71494) and apatite-II (0.70767–0.71585) show a large range values compared to those of the Tongling intrusive rocks (Fig. 12). Previous studies of these Tongling intrusive rocks proposed that they were likely

originated from the partial melting of subducted ocean slab and overlying sediments (e.g., Ling et al. 2009; Liu et al. 2010; Sun et al. 2011; Li et al. 2014). On the other hand, the $^{87}Sr/^{86}Sr$ ratios of apatite grains can record more detailed information than the whole-rock Sr isotopic compositions. Hence, the studied apatite grains with high $^{87}Sr/^{86}Sr$ ratios likely reflect the information of the overlying sediments, whereas apatite grains with similar $^{87}Sr/^{86}Sr$ ratios to those of whole-rock might record information of the homogenized magma. In addition, the involvement of subducted ocean slab and overlying sediments for the studied granitoids is confirmed by the binary plot of La/Sm versus Sr/Th ratios of apatite from the Tongling intrusive rocks (Fig. 14). In general, the intrusive rocks of the Tongling region, including the Shatanjiao granodiorites, are sourced from partial melting of subducted ocean slab and sediments. Meanwhile, Sr isotopes and trace element compositions of apatite can keep the essential information of the magma source.

5.3 Estimation on magma temperature and oxygen fugacity

Temperature and oxygen fugacity are important indexes for the magma melt because it has a huge influence on the nature and melting process of magma melt as well as the geochemical behavior of multivalent elements in the melt (Watson and Harrison 1983, 2005; Miller et al. 2003; Ferry and Watson 2007; Hayden and Watson 2007; Trail et al. 2012; Sun et al. 2013). Moreover, the oxygen fugacity has a great impact on the metallic mineralization. For example, low oxygen fugacity is essential for Sn–W mineralization, whereas high oxygen fugacity is one of the key factors for the porphyry Cu–Au mineralization (Lehmann 1982, 1990; Linnen et al. 1995, 1996;

346 Sun et al. 2013). Previous studies have proposed that some specific elements in zircon
347 and apatite are sensitive to the temperature and redox conditions of the melt, which
348 can be used as a valid tracer to reflect the physico-chemical conditions of the melt
349 (e.g., Harrison and Watson 1984; Sha and Chappell 1999; Ballard et al. 2002; Ferry
350 and Watson 2007; Trail et al. 2012; Miles et al. 2014). Using the model of zircon Ti
351 thermometer proposed by Ferry and Watson (2007), zircon grains from the
352 granodiorite samples (STJ01 and STJ09) have overlapping estimated temperatures
353 ranging from 581 to 720 °C (mean T = 653 °C) and 607 to 689 °C (mean T = 639 °C),
354 respectively (Fig. 15).

355 In terms of oxygen fugacity of the melt, the Ce^{4+}/Ce^{3+} ratios of zircon and Mn
356 contents in apatite are widely applied for estimating the oxygen fugacity of melt (Sha
357 and Chappell 1999; Ballard et al. 2002; Belousova et al. 2002; Miles et al. 2014).
358 Based on the model proposed by Ballard et al. (2002), the Ce^{4+}/Ce^{3+} ratios of zircon
359 grains from the granodiorite samples (STJ01 and STJ09) range from 55 to 445 (mean
360 = 245) and 181 to 939 (mean = 437), respectively (Table 2). These relatively high
361 Ce^{4+}/Ce^{3+}ratios are consistent with those of the Dexing porphyry deposit, which is
362 well accepted for its high oxygen fugacity (Fig. 16; Zhang et al. 2017). Since Mn^{2+} is
363 favored by apatite through substitution for Ca^{2+}, oxidized magma increases Mn^{4+} at
364 the expense of Mn^{2+} in the melt, resulting in low Mn concentration of apatite (Sha and
365 Chappell 1999; Belousova et al. 2002). In this study, both apatite-I and apatite-II have
366 low MnO contents varying between 0.06-0.07 wt % and 0.04-0.07 wt %, respectively.
367 Based on the model proposed by Miles et al. (2014), the calculated Log$f(O_2)$ values of

368 apatite-I and apatite-II are ranging from -9.90 to -9.88 and from -9.87 to -9.82,
369 respectively. These results consistently suggest that the zircon and apatite grains from
370 the studied granodiorites were formed in an oxidized magma melt. It should be noted
371 that oxidized magma is favorable for the Cu–Au mineralization (Sun et al. 2011, 2013;
372 Zhang et al. 2017), which corroborates the widespread occurrence of Cu–Au deposits
373 in the Shatanjiao region (see Fig. 3).

374 **5.4 Multi-stage magma evolutionary history**

375 The chemical composition of igneous rocks is mainly determined by the
376 multi-stage magma processes in deep crust, including melting, fractional
377 crystallization and assimilation (Hildreth and Moorbath, 1988; Annen et al. 2006;
378 Davidson et al. 2007). The adakite-like rocks mostly show features of high Sr, low Y
379 and Yb, high Sr/Y ratios, and lack of negative Eu anomalies, which might be caused
380 by intense fractional crystallization of amphibole (±garnet) and suppressed fractional
381 crystallization of plagioclase (Müntener et al. 2001; Zhang et al. 2001). Apatite is a
382 common accessory mineral in igneous rocks, and has the ability to reflect the
383 geochemical signatures of the discrete stages of melt (Jennings et al. 2011; Bruand et
384 al. 2016; Nathwani et al. 2020). As the major Sr reservoir, plagioclase contains high Sr
385 content and the fractional crystallization of plagioclase will have significant impact on
386 the Sr content of the melt. It was proposed that apatite can record the Sr content of the
387 melt at the time of its crystallization (Jennings et al. 2011; Bruand et al. 2016).
388 Crystallization of plagioclase will decrease the Sr content in the residual melt,
389 therefore, the early crystallized apatite will have high Sr content compared to that of

390 the lately crystallized apatite (Pan et al. 2016). In this study, apatite-I has higher Sr
391 content of 754–1242 ppm than apatite-II of 415–612 ppm, indicating that apatite-I
392 might have crystallized earlier than apatite-II. In addition, apatite-I has high contents
393 of MgO and FeO, and low contents of SiO_2 and ΣREE compared to those of apatite-II,
394 showing an acid magma evolution trend (Figs. 9a–9d). The studied granodiorite
395 samples have similar zircon U–Pb ages, making that it is unable to distinct the
396 magmatic episodes of the Shatanjiao pluton. Therefore, apatite might provide a new
397 tool to better constrain the different stages of magma evolution.

398 Plagioclase is a natural Eu reservoir, and plays an important role in Eu content of
399 the melt because the fractional crystallization of plagioclase will not only decrease Sr
400 but also Eu content in the residual melt (Bédard 2006; Bindeman and Davis 2020;
401 Dygert et al. 2020). In this study, apatite-I has high Eu/Eu* ratios of 0.56–0.76 than
402 apatite-II of 0.39–0.58, although both apatite group display a similar trend between
403 Eu/Eu* and Sr contents (Fig. 9e), indicating that more intense plagioclase fractional
404 crystallization occurred at the latter magmatic stage. Both apatite-I and apatite-II from
405 the studied graonodiorites are characterized by LREE enrichment and HREE
406 depletion, showing similar REE patterns to those of the Shatanjiao intrusive rocks
407 (Fig. 11), but apatite-I has much lower $(La/Yb)_N$ ratios (7.85–28.6) than those of
408 apatite-II (95.9–132) (Table 3; Fig. 9f), indicating that more intense HREE depletion
409 occurs in the latter stage melt. It should be noted that fractional crystallization some
410 specific minerals (e.g., garnet, hornblende and zircon) can attribute to the HREE
411 depletion of the melt (Sisson 1994; Otamendi and Patiño Douce 2001; Brophy et al.

412 2011; Fornelli et al. 2014, 2018). Continuous fractional crystallization these minerals
413 in the magma chamber leads to formation of melts with different REE features which
414 are likely the inherited by apatite. Therefore, apatite might be an efficient mineral to
415 record the magma evolution history.

416 6. IMPLICATIONS

417 The Shatanjiao granodiorites, formed in Late Jurassic, have similar geochemical
418 characteristics to the adakite-like rocks. This suggests a high oxygen fugacity and
419 temperature environment for the formation of the magma, which was likely originated
420 from the subducted oceanic crust. Considering the trace element composition of
421 apatite from the studied granodiorites, their high Sr contents indicate a source from
422 the early stage of magma evolution, whereas their low Sr contents suggest a formation
423 during the late stage of magma evolution. In addition, fractional crystallization of
424 plagioclase, garnet, hornblende and zircon might control the trace element
425 composition of melt during the magma evolutionary history, which were recorded by
426 the apatite.

427 ACKNOWLEDGMENTS

428 This work was financed by the National Key Research and Development Plan
429 (Grant No. 2018YFC0603902) and the National Key R&D Program of China (No.
430 2016YFC0600404).

431 REFERENCES

432 Andersen, T. (2002) Correction of common lead in U–Pb analyses that do not report

204Pb. Chemical Geology, 192, 59–79.

Annen, C., Blundy, J.D., and Sparks, R.S.J. (2006) The genesis of intermediate and silicic magmas in deep crustal hot zones. Journal of Petrology, 47, 505–539.

Ballard, J.R., Palin, J.M. and Campbell, I.H. (2002) Relative oxidation states of magmas inferred from Ce(IV)/Ce(III) in zircon: application to porphyry copper deposits of northern Chile. Contributions to Mineralogy and Petrology, 144, 347–364.

Bédard, J.H. (2006) Trace element partitioning in plagioclase feldspar. Geochimica et Cosmochimica Acta, 70, 3717–3742.

Belousova, E.A., Griffin, W.L., O'Reilly, S.Y., and Fisher, N.I. (2002) Apatite as an indicator mineral for mineral exploration: trace-element composition and their relationship to hostrock type. Journal of Geochemical Exploration, 76, 45–69

Berglund, M. and Wieser, M.E. (2011) Isotopic compositions of the elements 1997 (IUPAC Technical Report). Pure and Applied chemistry, 83, 397–410

Bindeman, I.B., and Davis, A.D. (2020) Trace element partitioning between plagioclase and melt: investigation of dopant influence on partition behavior. Geochimica et Cosmochimica Acta, 64, 2864-2878.

Brophy, J.G., Ota, T., Kunihro, T., Tsujimori, T., Nakamura, E. (2011) In situ ion-microprobe determination of trace element partition coefficients for hornblende, plagioclase, orthopyroxene, and apatite in equilibrium with natural rhyolitic glass, Little Glass Mountain Rhyofite, California. American Mineralogist, 96, 1838–1850.

455 Bruand, E., Fowler, M., Storey, C., and Darling, J. (2017) Apatite trace element and
456 isotope applications to petrogenesis and provenance. American Mineralogist, 102,
457 75–84.
458 Bruand, E., Storey, C., and Fowler, M. (2016) An apatite for progress: Inclusions in
459 zircon and titaniteconstrain petrogenesis and provenance. Geology,44, 91–94.
460 Cao, Y., Gao, F.P., Du, Y.S., Du, Y.L., and Pang, Z.S. (2017) Genesis of the
461 Datuanshan stratabound skarn Cu(-Mo) deposit, Middle-Lower Yangtze Valley,
462 Eastern China: constraints from geology, Re-Os geochronology, mineralogy,
463 and sulfur isotopes. Mineralium Deposita, 52, 443–462.
464 Chang, Y.F., Liu, X.P., and Wu, Y.C., 1991. The copper–iron belt along the middle and
465 lower reaches of the Changjiang River. Geological Publishing House, Beijing.
466 379 pp. (in Chinese with English abstract).
467 Chen, C.J., Chen, B., and Wang, Z.Q. (2016) Important role of magma mixing in
468 generating the Mesozoic monzodioritic–granodioritic intrusions related to Cu
469 mineralization,Tongling, East China: Evidence from petrological and in situ
470 Sr-Hf isotopic data. Lithos, 248–251, 80–93.
471 Chen, J.F., Xie, Z., Zhang, X., and Zhou, T.X. (2001) Crustal evolution in Anhui: Nd
472 and Sr isotopic evidence. Geology of Anhui, 11, 123–130. (in Chinese with
473 English abstract)
474 Chen, L., Yan, Z., Wang, Z.Q., and Wang, K.M. (2017) Characteristics of apatite from
475 160–140 Ma Cu(Mo) and Mo(W) deposits in East Qinling. Acta Geologica.
476 Sinica. 91, 1925–19402. (in Chinese with English abstract)

Chiaradia, M. (2009) Adakite-like magmas from fractional crystallization and melting-assimilation of mafic lower crust (Eocene Macuchi arc, Western Cordillera, Ecuador). Chemical Geology, 265, 468–487.

Davidson, J., Turner, S., Handley, H., Macpherson, C., and Dosseto, A. (2007) Amphibole "sponge"in arc crust? Geology, 35, 787–790.

Defant, M.J., and Drummond, M.S. (1990) Derivation of some modern arc magmas by melting of young subducted lithosphere. Nature 347, 662–665.

Defant, M.J., and Drummondount, M.S. (1993) St. Helens: Potential example of the partial melting of the subducted lithosphere in a volcanic arc. Geology, 21(6), 547–550.

Dygert, N., Draper, D.S., Rapp, J.F., Lapen, T.J., Fagan, A.L., and Neal, C.R. (2020) Experimental determinations of trace element partitioning between plagioclase, pigeonite, olivine, and lunar basaltic melts and an fO(2) dependent model for plagioclase-melt Eu partitioning. Geochimica et Cosmochimica Acta, 279, 258–280.

Erwan, B., Jean-Philippe, E., Michel, M., Claude, R., Herve, M., Joseph, C., and Minard, L.H. (2002) Adakite-like lavas from Antisana volcano (Ecuador): Evidence for slab melt metasomatism beneath Andean Northern Volcanic Zone. Journal of Petrology, 43, 199–217.

Ferry, J.M., and Watson, E.B. (2007) New thermodynamic models and revised calibrations for the Ti-in-zircon and Zr-in-rutile thermometers. Contributions to Mineralogy and Petrology, 154, 429–437.

Fornelli, A., Langone, A., Micheletti, F., and Piccarreta, G. (2018) REE partition among zircon, orthopyroxene, amphibole and garnet in a high-grade metabasic system. Geological Magazine, 155, 1705–1726.

Fornelli, A., Langone, A., Micheletti, F., Pascazio, A., and Piccarreta, G. (2014) The role of trace element partitioning between garnet, zircon and orthopyroxene on the interpretation of zircon U-Pb ages: an example from high-grade basement in Calabria (Southern Italy). International Journal of Earth Sciences, 103, 487–507.

Gao, S., Ling, W.L., Qiu, Y.M., Lian, Z., Hartman, G., and Simon, K. (1999) Contrasting geochemical and Sm-Nd isotopic compositions of Archean metasediments from the Kongling high-grade terrain of the Yangtze craton: Evidence for cratonic evolution and redistribution of REE during crustal anataxis. Geochimica Et Cosmochimica Acta, 63, 2071–2088.

Gao, S., Yang, J., Zhou, L., Li, M., Hu, Z.C., Guo, J.L., Yuan, H.L., Gong, H.J., Xiao, G.Q., and Wei, J.Q. (2011) Age and growth of the Archean Kongling Terrain, South China, with emphasis on 3.3 Ga granitoid gneisses. American Journal of Science, 311, 153–182.

Gao, Y., Hou, Z., Kamber, B.S., Wei, R., Meng, X., and Zhao, R.(2007)Adakite-like porphyries from the southern Tibetan continental collision zones: Evidence for slab melt metasomatism. Contributions to Mineralogy and Petrology, 153(1), 105–120.

Guo, J.L., Gao, S., Wu, Y.B., Li, M., Chen, K., Hu, Z.C., Liang, Z.W., Liu, Y.S., Zhou,

L., Zong, K.Q., Zhang, W., and Chen, H.H. (2014) 3.45 Ga granitic gneisses from the Yangtze Craton, South China: Implications for Early Archean crustal growth. Percambrian Research, 242, 82–95.

Harrison, T.M., and Watson, E.B., 1984. The behavior of apatite during crnstal anatexis: Equilibrium and kinetic considerations. Geochimica et Cosmochimica Acta, 48, 1467–1477.

Hayden, L.A. and Watson, E.B. (2007) Rutile saturation in hydrous siliceous melts and its bearing on Ti-thermometry of quartz and zircon. Earth and Planetary Science Letters, 258, 561–568.

Hildreth, W., and Moorbath, S. (1988) Crustal contributions to arc magmatism in the Andes of CentralChile. Contributions to Mineralogy and Petrology, 98, 455–489.

Hoskin, P.W.O., and Schaltegger, U. (2003) The composition of zircon and igneous and metamorphic petrogenesis. Reviews in Mineralogy and Geochemistry, 53, 27–62.

Hu, Z.C., Zhang, W., Liu, Y.S., Gao, S., Li, M., Zong, K.Q., Chen, H.H., and Hu, S.H. (2015) “Wave” signal smoothing and mercury removing device for laser ablation quadrupole and multiple collector ICP–MS analysis: application to lead isotope analysis. Analytical Chemistry, 87, 1152–1157.

Jennings, E.S., Marschall, H.R., Hawkesworth,C.J., and Storey, C.D. (2011) Characterization of magma from inclusions in zircon: Apatite and biotite work well, feldspar less so. Geology, 39, 863–866.

Li, S., Yang, X.Y., Yu, H., and Sun, W.D.(2014) Petrogenesis and mineralization of the Fenghuangshan skarn Cu-Au deposit,Tongling ore cluster field, Lower Yangtze metallogenic belt. Ore Geology Reviews, 58, 148–162.

Linnen, R.L., Pichavant, M., and Holtz, F. (1996) The combined effects of fO_2 and melt composition on SnO_2 solubility and tin diffusivity in haplogranitic melts. Geochimica et Cosmochimica Acta, 60, 4965–4976.

Linnen, R.L., Pichavant, M., Holtz, F., and Burgess, S. (1995) The effect of fO2 on the solubility, diffusion, and speciation of tin in haplogranitic melt at 850 °C and 2 kbar. Geochimica et Cosmochimica Acta, 59, 1579–1588.

Liu, S.A., Li, S.G., He, Y.S., and Huang, F. (2010) Geochemical contrasts between early Cretaceous ore-bearing and ore barren high-Mg adakites in central-eastern China: Implications for petrogenesis and Cu-Au mineralization. Geochimica et Cosmochimica Acta, 74, 7160–7178.

Liu, Y.S., Gao, S., Hu, Z.C., Gao, C.G., Zong, K.Q., and Wang, D.B.(2010) Continental and oceanic crust recycling-induced melt-peridotite interactions in the Trans-North China Orogen: U–Pb dating, Hf isotopes and trace elements in zircons of mantle xenoliths. Journal of Petrology, 51, 537–571.

Liu, Y.S., Hu, Z.C., Gao, S., Gu¨ ther, D., Xu, J., Gao, C.G., and Chen, H.H.(2008) In situ analysis of major and trace elements of anhydrous minerals by LA–ICP–MS without applying an internal standard. Chemical Geology, 257, 34–43.

Liu, Z.F., Shao, Y.J., Zhang, Y., and Wang, C. (2018). Geochemistry and geochronology of the Qingshanjiao granites: Implications for the genesis of the

565 Dongguashan copper (gold) ore deposit in the Tongling ore district, Eastern
566 China. Ore Geology Reviews, 99, 42–57.
567 Ludwig, K.R. (2003) ISOPLOT 3.00: A Geochronological Toolkit for Microsoft Excel.
568 Berkeley Geochronology Center, Berkeley, California, 39 pp.
569 Macpherson, C.G., Dreher, S.T., and Thirlwall, M.F. (2006) Adakites without slab
570 melting: High pressure differentiation of island arc magma, Mindanao, the
571 Philippines. Earth and Planetary Science Letters, 243(3-4), 581–593.
572 Mao, J.W., Shao, Y.J., Xie, G.Q., Zhang, J.D., and Chen, Y.C. (2009) Mineral deposit
573 model for porphyry-skarn polymetallic copper deposits in Tongling ore dense
574 district of MiddleLower Yangtze Valley metallogenic belt. Mineral Deposits, 28,
575 109–119. (in Chinese with English abstract)
576 Martin, H. (1999) The adakitic magmas: modern analogues of Archaean granitoids.
577 Lithos, 46, 411–429.
578 Martin, H. (1999) The adakitic magmas: modern analogues of Archaean granitoids.
579 Lithos, 46, 411– 429.
580 Martin, H., Smithies, R. H., Rapp, R., Moyen, J. F., and Champion, D. (2005) An
581 overview of adakite, tonalite-trondhjemite-granodiorite (TTG), and sanukitoid:
582 relationships and some implications for crustal evolution. Lithos, 79, 1–24.
583 Miles A.J., Graham C. M., Hawkesworth, C., Gillespie M.R., Hinton R.W. and
584 Bromiley G.D. (2014) Apatite: a new redox proxy for silicic magmas?
585 Geochimica et Cosmochimica Acta,132, 101–119.
586 Miller, C.F., McDowell, S.M., and Mapes, R.W. (2003) Hot and cold granites?

587 Implications of zircon saturation temperatures and preservation of inheritance.
588 Geology, 31, 529–532.
589 Müntener, O., Kelemen, P.B., and Grove, T.L. (2001) The role of H_2O during
590 crystallization of primitive arc magmas under uppermost mantle conditions and
591 genesis of igneous pyroxenites: An experimental study. Contributions to
592 Mineralogy and Petrology, 141, 643–658.
593 Nathwani, C.L., Loader, M.A., Wilkinson, J.J., Buret, Y., Sievwright, R.H., and
594 Holling, P. (2020) Multi-stage arc magma evolution recorded by apatite in
595 volcanic rocks. Geology, 48, 323–327.
596 Otamendi, J.E., and Patiño Douce, A.E. (2001) Partial melting of aluminous
597 metagreywackes in the northern Sierra de Comechingones, central Argentina.
598 Journal of Petrology, 42, 1751–1772.
599 Pan, L.C., Hu, R.Z., Wang, X.S., Bi, X.W., Zhu, J.J., and Li, C.S. (2016) Apatite trace
600 element and halogen compositions as petrogenetic-metallogenic indicators:
601 Examples from four granite plutons in the Sanjiang region, SW China. Lithos,
602 254-255, 118–130.
603 Pan, Y.M., and Dong, P. (1999) The lower Changjiang (Yangzi/Yangtze River)
604 metallogenic belt, East Central China: intrusion- and wall rock-hosted
605 Cu-Fe-Au, Mo, Zn, Pb, Ag deposits. Ore Geology Reviews, 15, 177–242
606 Pan, Y.Y., and Fleet, M.E. (2002) Compositions of the Apatite-Group Minerals:
607 Substitution Mechanisms and Controlling Factors: Geochemical, Geobiological
608 and Materials Importance. Phosphates.

609 Prowatke, S., and Klemme, S. (2006) Rare earth element partitioning between titanite
610 and silicate melts: Henry's law revisited. Geochimica et Cosmochimica Acta 70,
611 4997–5012.
612 Richards, J.P., and Kerrich, R. (2007) Special Paper: Adakite-Like Rocks: Their
613 Diverse Origins and Questionable Role in Metallogenesis. Economic Geology,
614 102, 537-576.
615 Rollinson, H. (1993) Using Geochemical Data: Evaluation, Presentation,
616 Interpretation. Longman, London. 352.
617 Sha, L.K., and Chappell, B.W. (1999) Apatite chemical composition, determined by
618 electron microprobe and laser-ablation inductively coupled plasma mass
619 spectrometry, as a probe into granite petrogenesis-some mineralogical and
620 petrological constraints. Geochimica et Cosmochimica Acta, 63, 3861–3881.
621 Sisson, T.W. (1994) Hornblende-melt trace-element partitioning measured by Ion
622 Microprobe. Chemical Geology, 117, 331–344.
623 Sun, W., Liang, H., Ling, M., Zhan, M., Ding, X., Zhang, H., Yang, X., Li, Y., Ireland,
624 T.R., Wei, Q., and Fan, W. (2013) The link between reduced porphyry copper
625 deposits and oxidized magmas. Geochimica et Cosmochimica Acta, 103,
626 263–275.
627 Sun, W.D., Ling, M.X., Ding, X., Chung, S.L., Zhou, J.B., Yang, X.Y., and Fan, W.M.
628 (2011) The association between adakites and Cu-Au ore deposits. International
629 Geology Review, 53, 691–703.
630 Taylor, S.R., and McLennan, S.M. (1985) Continental crust: its composition and

631 evolution. An examination of the geochemical record preserved in sedimentary
632 rocks. Blackwell Science Inc, Boston, pp. 312.
633 Tong, X.R., Liu, Y.S., Hu, Z.C., Chen, H.H., Zhou, L., Hu, Q.H., Xu, R., Deng, L.X.,
634 Chen, C.F., and Yang, L. (2016) Accurate Determination of Sr Isotopic
635 Compositions in Clinopyroxene and Silicate Glasses by LA–MC–ICP–MS.
636 Geostandards and Geoanalytical Research, 40, 85–99.
637 Trail, D., Watson, E.B., and Tailby, N.D. (2012) Ce and Eu anomalies in zircon as
638 proxies for the oxidation state of magmas. Geochimica et Cosmochimica Acta,
639 97, 70–87.
640 Trail, D., Watson, E.B., and Tailby, N.D. (2012) Ce and Eu anomalies in zircon as
641 proxies for the oxidation state of magmas. Geochimica et Cosmochimica Acta
642 97, 70–87.
643 Tsuboi, M. (2005) The use of apatite as a record of initial $^{87}Sr/^{86}Sr$ ratios and indicator
644 of magma processes in the Inagawa pluton, Ryoke belt, Japan. Chem. Geol. 221,
645 157–169.
646 Tsuboi, M., Suzuki, K., 2003. Heterogeneity of initial $^{87}Sr/^{86}Sr$ ratios within a single
647 pluton: evidence from apatite strontium isotopic study. Chem. Geol. 199,
648 189–197.
649 Wang, Y.Y., Wang, X.S., Bi, X.W., Tao, Y., and Lan, T.G. (2019) Intraplate
650 adakite-like rocks formed by differentiation of mantle-derived mafic magmas: A
651 case study of Eocene intermediate-felsic porphyries in the Machangqing
652 porphyry Cu-Au mining district, SE Tibetan plateau. Journal of Asian Earth

653 Sciences, 196, 104364.

654 Watson, E.B., and Green, T.H. (1981) Apatite/liquid partition coefficients for the rare
655 earth elements and strontium. Earth and Planetary Science Letters, 56, 405–421.

656 Watson, E.B., and Harrison, T.M. (1983) Zircon saturation revisited: temperature and
657 composition effects in a variety of crustal magma types. Earth and Planetary
658 Science Letters, 64, 295–304.

659 Watson, E.B., and Harrison, T.M. (2005) Zircon thermometer reveals minimum
660 melting conditions on earliest Earth. Science, 308, 841–844.

661 Wei, Y.X., Zhou, W.X., Hu, Z.X., Li, H.Q., Huang, X.X., Zhao, X.M., Xu, D.L. (2019)
662 Geochronology and Geochemistry of Archean TTG and Tremolite Schist
663 Xenoliths in Yemadong Complex: Evidence for >= 3.0 Ga Archean Continental
664 Crust in Kongling High-Grade Metamorphic Terrane, Yangtze Craton, China.
665 Minerals, 9, 689.

666 Wu, X.X., Yan, J., Tang, Y.L., Chu, X.Q., and Peng, G. (2011). Geochronology and
667 Geochemistry of Shatanjiao granodiorite from Tongling, Anhui Province.
668 Mineralogy and Petrology, 31, 75–82. (in Chinese with English abstract)

669 Xiao, X., Zhou, T.F., White, N.C., Zhang, L.J., Fan, Y., and Chen, X.F. (2020)
670 Multiple generations of titanites and their geochemical characteristics record
671 the magmatic-hydrothermal processes and timing of the Dongguashan
672 porphyry-skarn Cu-Au system, Tongling district, Eastern China. Mineralium
673 Deposita (DOI: 10.1007/s00126-020-00962-0).

674 Xie, J.C., Wang, Y., Li, Q.Z., Yan, J., and Sun, W.D. (2017). Petrogenesis and

675 metallogenic implications of Late Mesozoic intrusive rocks in the Tongling
676 region, eastern China: a case study and perspective review. International
677 Geology Review, 60, 1361–1380.
678 Yang, X.N., Wu, Z.W., Lu, X.C., Jiang, S.Y., Ling, H.F., Liu, L.G., and Chen, D.Y.
679 (2011) Porphyry and skarn Au–Cu deposits in the Shizishan orefield, Tongling,
680 East China:U–Pb dating and in-situ Hf isotope analysis of zircons and
681 petrogenesis of associated granitoids. Ore Geology Reviews, 43, 182–193.
682 Yang, Y.H., Wu, F.Y., Yang, J.H., Chew, D.M., Xie, L.W., Chu, Z.Y., Zhang, Y.B.,
683 and Huang, C. (2014) Sr and Nd isotopic compositions of apatite reference
684 materials used in U–Th–Pb geochronology. Chemical Geology, 385, 35–55.
685 Zhang, C.C., Sun, W.D., Wang, J.T., Zhang, L.P., Sun, S.J., and Wu, K.(2017) Oxygen
686 fugacity and porphyry mineralization: A zircon perspective of Dexing porphyry
687 Cu deposit, China. Geochimica et Cosmochimica Acta, 206, 343–363.
688 Zhang, S.B., Zheng, Y.F., Wu, Y.B., Gao, S., and Wu, F.W. (2006). Zircon isotope
689 evidence for >= 3.5 Ga continental crust in the Yangtze craton of China.
690 Precambrian Research, 146, 16–34.
691 Zhong, G.X., Zhou, T.F., Yuan, F., Jiang, Q.S., Fan, Y., Zhang, D.Y., and Huang, J.M.
692 (2014) LA–ICPMS U–Pb zircon age and molybdenite Re-Os dating of
693 Yaojialing large zinc-gold polymetallic deposit, Tongling, Anhui Province,
694 China. Acta Petrologica Sinica, 30, 1075–1086.
695 Zong, K.Q., Klemd, R., Yuan, Y., He, Z.Y., Guo, J.L., Shi, X.L., Liu, Y.S., Hu, Z.C.,
696 and Zhang, Z.M.(2017) The assembly of Rodinia: The correlation of early

Neoproterozoic (ca. 900 Ma) high-grade metamorphism and continental arc formation in the southern Beishan Orogen, southern Central Asian Orogenic Belt (CAOB). Precambrian Research, 290, 32–48.

FIGURE CAPTIONS

FIGURE 1. Regional geological sketch map showing the distribution of major mining districts along the Yangtze River in East China, and the location of the Shatanjiao pluton (modified from Pan and Dong, 1999).

FIGURE 2. Geological map and distribution of magmatic pluton in the Tongling region, Anhui (Mao et al. 2009)

FIGURE 3. Geological sketch map of the Shatanjiao region, showing the sampling location.

FIGURE 4. Hand specimens and photomicrographs of representative granitoids from the Shatanjiao pluton: (a–b) Medium to coarse grained granodiorite and (c–d) fine to medium grained granodiorite. Bt–biotite; Hbl–hornblende; Kfs–K-feldspar; Pl–plagioclase; Qtz–quartz.

FIGURE 5. CL images of representative zircon grains from the Shatanjiao granodiorites, showing the location of analyzed spot and corresponding U–Pb age.

FIGURE 6. Zircon U–Pb concordia diagram and weighted-mean ages of

representative zircon grains from the Shatanjiao granodiorites.

FIGURE 7. Rare earth element distributions in zircon from the Shatanjiao granodiorite. Chondrite normalization based on Taylor and McLennan (1985).

FIGURE 8. BSE images of representative apatite grains from the Shatanjiao granodiorites.

FIGURE 9. Geochemical diagrams of representative elements and parameters of apatite from the Shatanjiao granodiorites.

FIGURE 10. SiO_2 versus MnO diagram for the apatite from the Shatanjiao granodiorites (modified from Chen et al. 2017) .

FIGURE 11. Rare earth element distributions in apatite from the Shatanjiao granodiorites. Chondrite normalization based on Taylor and McLennan (1985).

FIGURE 12. Sr isotopic compositions of the apatite from the Shatanjiao granodiorites. The data of the intrusive rocks in the Tongling region were from Chen et al. (2016).

FIGURE 13. Plot of Eu/Eu* versus Sr/Y for apatite hosted in the Shatanjiao granodiorites (modified from Pan et al. 2016).

FIGURE 14. La/Sm versus Sr/Th for apatite from the Shatanjiao granodiorites and

746 other granitoids in the Tongling region (modified from Ding et al. 2015).

747

748 **FIGURE 15.** Histogram of calculated temperatures of zircon grains from the
749 Shatanjiao granodiorites.

750

751 **FIGURE 16.** Eu/Eu* versus Ce^{4+}/Ce^{3+} for zircon grains from the Shatanjiao
752 granodiorites. Data for porphyry (ore-barren and ore-bearing) in Chile, and Dexing
753 porphyry are from Ballard et al. (2002) and Zhang et al. (2017), respectively.

754

This is the peer-reviewed, final accepted version for American Mineralogist, published by the Mineralogical Society of America.
The published version is subject to change. Cite as Authors (Year) Title. American Mineralogist, in press.
DOI: https://doi.org/10.2138/am-2021-7871. http://www.minsocam.org/

Table 1. LA–MC–ICPMS zircon U–Pb isotopic dating data for the Shatanjiao granodiorites

Spot No.	Th	U	Th/U	$^{207}Pb/^{206}Pb$		$^{207}Pb/^{235}U$		^{206}Pb
	ppm	ppm		Ratio	2sigma	Ratio	2sigma	Ratio
Fine- to medium-grained granodiorite (sample STJ01)								
STJ01-1	222	409	0.54	0.0500	0.0086	0.1505	0.0244	0.0221
STJ01-2	182	467	0.39	0.0479	0.0115	0.1507	0.0338	0.0228
STJ01-3	105	345	0.31	0.0493	0.0062	0.1513	0.0187	0.0223
STJ01-4	120	362	0.33	0.0497	0.0071	0.1513	0.0221	0.0220
STJ01-5	73	265	0.28	0.0494	0.0079	0.1521	0.0247	0.0224
STJ01-6	94	329	0.29	0.0478	0.0116	0.1533	0.0441	0.0226
STJ01-7	104	377	0.28	0.0489	0.0082	0.1480	0.0253	0.0219
STJ01-8	89	317	0.28	0.0505	0.0066	0.1564	0.0201	0.0225
STJ01-9	199	467	0.43	0.0487	0.0083	0.1521	0.0246	0.0228
STJ01-10	90	319	0.28	0.0493	0.0098	0.1482	0.0302	0.0217
STJ01-11	78	292	0.27	0.0507	0.0083	0.1538	0.0252	0.0220
STJ01-12	69	276	0.25	0.0496	0.0140	0.1540	0.0397	0.0232
STJ01-13	137	451	0.30	0.0508	0.0050	0.1547	0.0153	0.0221
STJ01-14	131	432	0.30	0.0484	0.0061	0.1490	0.0195	0.0222
STJ01-15	122	348	0.35	0.0505	0.0081	0.1528	0.0247	0.0220
STJ01-16	127	421	0.30	0.0494	0.0068	0.1504	0.0199	0.0222
STJ01-17	124	321	0.39	0.0486	0.0074	0.1493	0.0230	0.0224
STJ01-18	178	459	0.39	0.0523	0.0063	0.1582	0.0178	0.0227
STJ01-19	214	481	0.44	0.0518	0.0074	0.1583	0.0220	0.0224
STJ01-20	177	440	0.40	0.0496	0.0069	0.1505	0.0215	0.0224
STJ01-21	303	651	0.47	0.0467	0.0072	0.1400	0.0208	0.0219
STJ01-22	196	515	0.38	0.0487	0.0075	0.1478	0.0245	0.0221
Medium- to coarse-grained granodiorite (sample STJ09)								
STJ09-1	82	201	0.41	0.0484	0.0097	0.1487	0.0293	0.0223
STJ09-2	76	220	0.34	0.0500	0.0082	0.1516	0.0239	0.0223
STJ09-3	256	356	0.72	0.0490	0.0100	0.1494	0.0319	0.0222
STJ09-4	127	210	0.61	0.0510	0.0091	0.1514	0.0276	0.0218
STJ09-5	72	173	0.41	0.0512	0.0100	0.1560	0.0313	0.0224
STJ09-6	305	384	0.80	0.0492	0.0082	0.1477	0.0257	0.0220
STJ09-7	75	182	0.41	0.0490	0.0101	0.1487	0.0294	0.0222
STJ09-8	240	317	0.75	0.0485	0.0064	0.1498	0.0214	0.0222
STJ09-9	151	344	0.44	0.0487	0.0066	0.1507	0.0211	0.0227
STJ09-10	220	298	0.74	0.0514	0.0069	0.1535	0.0200	0.0221
STJ09-11	144	237	0.61	0.0514	0.0092	0.1540	0.0262	0.0223
STJ09-12	164	295	0.56	0.0501	0.0072	0.1504	0.0221	0.0221
STJ09-13	169	306	0.55	0.0490	0.0067	0.1502	0.0211	0.0222
STJ09-14	207	290	0.71	0.0481	0.0069	0.1464	0.0201	0.0224
STJ09-15	112	191	0.59	0.0496	0.0126	0.1522	0.0347	0.0223
STJ09-16	132	178	0.74	0.0509	0.0121	0.1524	0.0317	0.0227
STJ09-17	222	260	0.85	0.0488	0.0071	0.1499	0.0230	0.0222
STJ09-18	96	178	0.54	0.0497	0.0102	0.1509	0.0292	0.0222
STJ09-19	167	265	0.63	0.0515	0.0066	0.1580	0.0210	0.0223
STJ09-20	185	289	0.64	0.0496	0.0065	0.1532	0.0209	0.0223
STJ09-21	81	232	0.35	0.0494	0.0110	0.1454	0.0335	0.0214
STJ09-22	261	411	0.63	0.0484	0.0058	0.1488	0.0184	0.0223
STJ09-23	251	316	0.79	0.0508	0.0073	0.1573	0.0232	0.0223

STJ09-24	275	365	0.75	0.0463	0.0056	0.1424	0.0176	0.0223
STJ09-25	160	267	0.60	0.0489	0.0075	0.1496	0.0233	0.0223

This is the peer-reviewed, final accepted version for American Mineralogist, published by the Mineralogical Society of America.
The published version is subject to change. Cite as Authors (Year) Title. American Mineralogist, in press.
DOI: https://doi.org/10.2138/am-2021-7871. http://www.minsocam.org/

$^{/238}$U	^{208}Pb/^{232}Th		^{207}Pb/^{206}Pb		^{207}Pb/^{235}U		^{206}Pb/^{238}U	
2sigma	Ratio	2sigma	Age (Ma)	2sigma	Age (Ma)	2sigma	Age (Ma)	2sigma
0.0011	0.0064	0.0006	195	359	142	22	141	7
0.0012	0.0068	0.0011	100	483	143	30	145	8
0.0009	0.0073	0.0008	161	270	143	17	142	6
0.0008	0.0071	0.0007	183	304	143	20	140	5
0.0013	0.0066	0.0009	169	337	144	22	143	8
0.0018	0.0079	0.0013	100	487	145	39	144	11
0.0015	0.0067	0.0009	146	352	140	22	140	10
0.0009	0.0072	0.0006	217	278	148	18	144	6
0.0010	0.0071	0.0007	132	356	144	22	145	6
0.0017	0.0065	0.0011	165	404	140	27	138	11
0.0010	0.0067	0.0008	228	341	145	22	140	6
0.0018	0.0067	0.0011	176	553	145	35	148	11
0.0008	0.0068	0.0006	232	211	146	13	141	5
0.0010	0.0072	0.0006	120	270	141	17	142	6
0.0011	0.0070	0.0007	217	333	144	22	140	7
0.0009	0.0068	0.0007	165	293	142	18	141	6
0.0011	0.0064	0.0007	128	326	141	20	143	7
0.0020	0.0071	0.0006	298	256	149	16	144	12
0.0015	0.0065	0.0006	276	296	149	19	143	9
0.0016	0.0064	0.0005	189	287	142	19	143	10
0.0019	0.0064	0.0006	35	333	133	18	140	12
0.0020	0.0064	0.0007	200	261	140	22	141	12
0.0016	0.0072	0.0010	117	415	141	26	142	10
0.0016	0.0069	0.0009	195	406	143	21	142	10
0.0018	0.0070	0.0007	146	418	141	28	141	11
0.0018	0.0064	0.0007	239	367	143	24	139	11
0.0020	0.0067	0.0009	250	394	147	27	143	12
0.0019	0.0066	0.0005	167	339	140	23	140	12
0.0017	0.0067	0.0007	146	426	141	26	142	10
0.0013	0.0068	0.0005	124	285	142	19	141	8
0.0015	0.0072	0.0007	132	302	143	19	145	9
0.0014	0.0067	0.0005	257	285	145	18	141	9
0.0017	0.0067	0.0006	257	376	145	23	142	11
0.0014	0.0069	0.0006	198	304	142	20	141	9
0.0011	0.0073	0.0006	150	293	142	19	142	7
0.0012	0.0072	0.0005	106	307	139	18	143	7
0.0020	0.0069	0.0008	176	507	144	31	142	12
0.0014	0.0075	0.0007	235	474	144	28	145	9
0.0011	0.0072	0.0005	200	250	142	20	142	7
0.0014	0.0072	0.0008	189	409	143	26	141	9
0.0011	0.0073	0.0006	261	270	149	18	142	7
0.0010	0.0074	0.0006	176	281	145	18	142	6
0.0016	0.0077	0.0012	169	448	138	30	136	10
0.0010	0.0071	0.0006	120	268	141	16	142	6
0.0010	0.0073	0.0006	235	365	148	20	142	6

0.0011	0.0069	0.0005	13	267	135	16	142	7
0.0011	0.0073	0.0007	143	335	142	21	142	7

This is the peer-reviewed, final accepted version for American Mineralogist, published by the Mineralogical Society of America.
The published version is subject to change. Cite as Authors (Year) Title. American Mineralogist, in press.
DOI: https://doi.org/10.2138/am-2021-7871. http://www.minsocam.org/

$^{208}Pb/^{232}Th$	
Age (Ma)	2sigma
128	12
137	22
148	16
142	13
134	18
159	26
135	19
146	13
142	13
130	21
135	17
135	22
137	11
146	12
140	14
136	14
129	15
142	12
131	12
128	11
128	13
128	14
145	20
139	18
141	13
129	14
135	17
133	11
135	14
138	10
145	13
134	10
136	12
139	12
148	13
146	10
139	17
150	14
146	10
145	16
148	11
149	12
155	24
144	12
147	12

140	11
146	13

This is the peer-reviewed, final accepted version for American Mineralogist, published by the Mineralogical Society of America.
The published version is subject to change. Cite as Authors (Year) Title. American Mineralogist, in press.
DOI: https://doi.org/10.2138/am-2021-7871. http://www.minsocam.org/

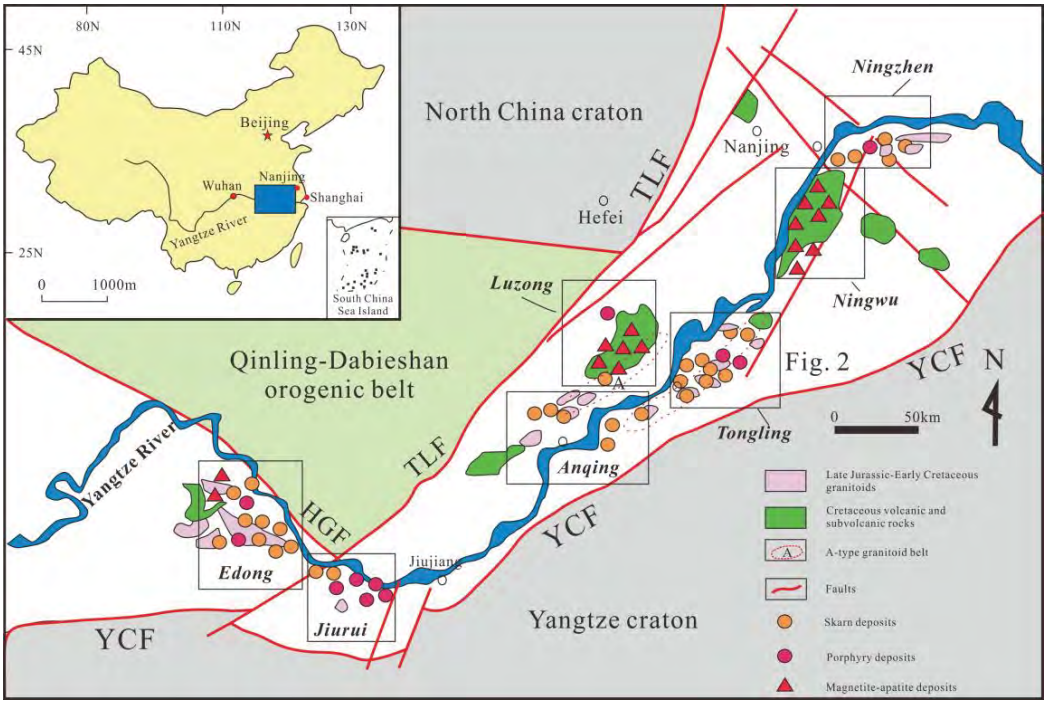

Figure 1

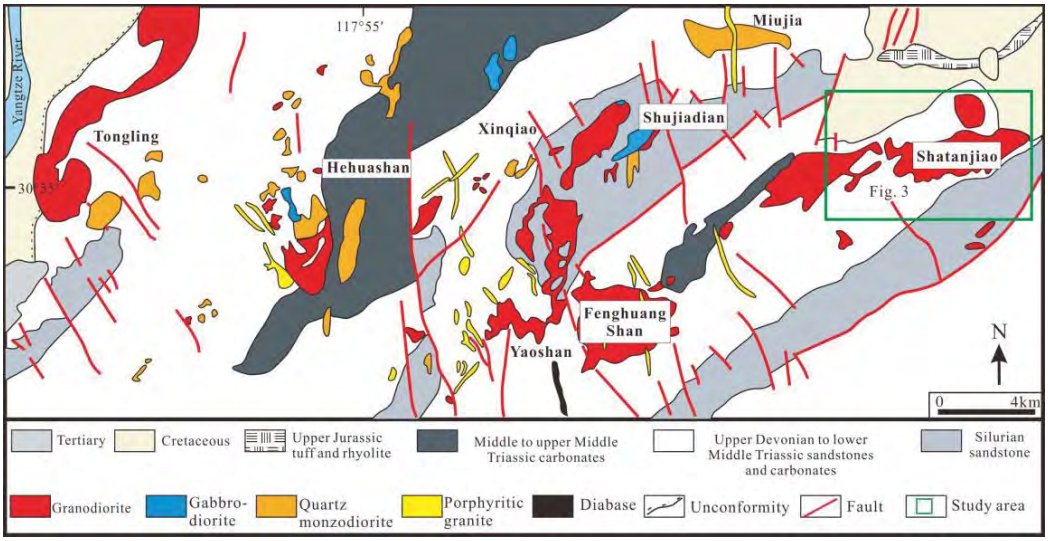

Figure 2

This is the peer-reviewed, final accepted version for American Mineralogist, published by the Mineralogical Society of America.
The published version is subject to change. Cite as Authors (Year) Title. American Mineralogist, in press.
DOI: https://doi.org/10.2138/am-2021-7871. http://www.minsocam.org/

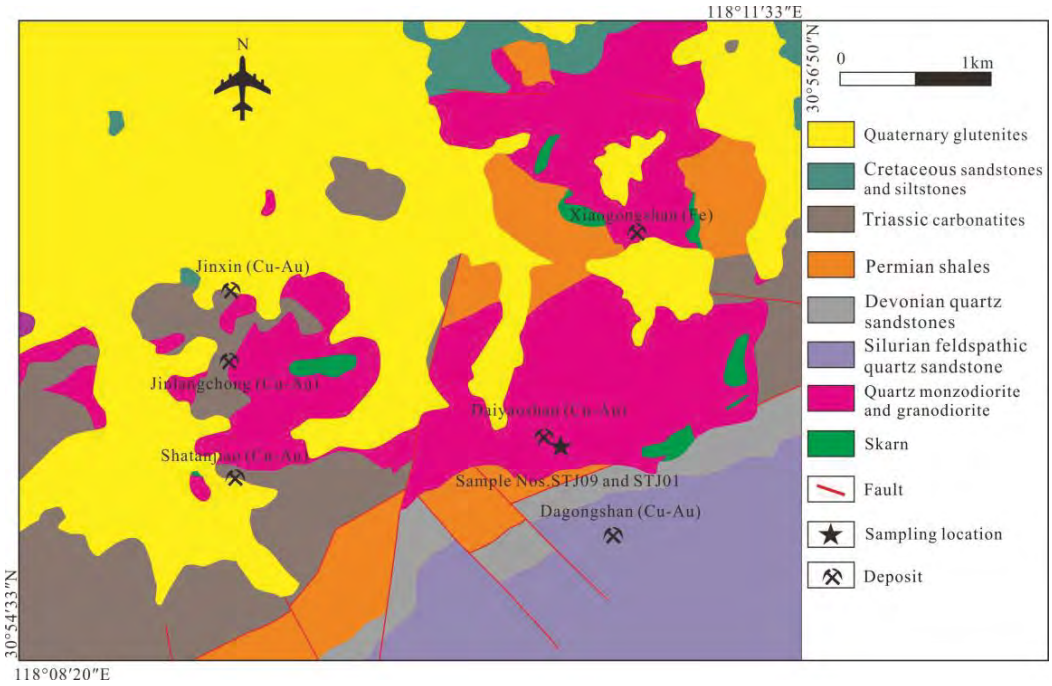

Figure 3

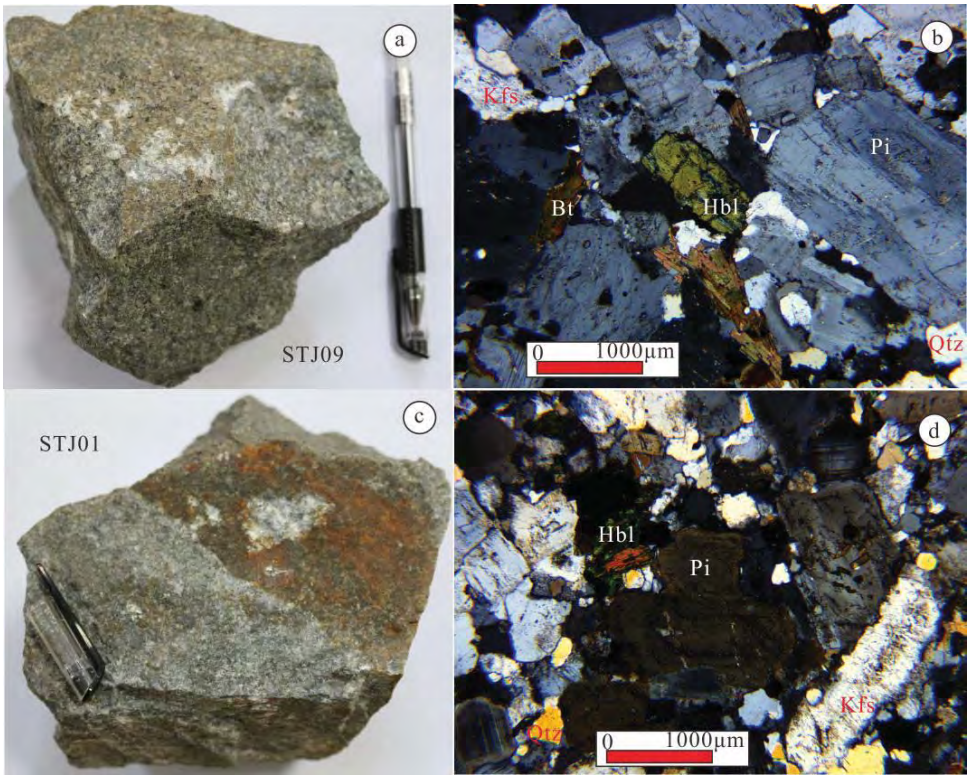

Figure 4

This is the peer-reviewed, final accepted version for American Mineralogist, published by the Mineralogical Society of America.
The published version is subject to change. Cite as Authors (Year) Title. American Mineralogist, in press.
DOI: https://doi.org/10.2138/am-2021-7871. http://www.minsocam.org/

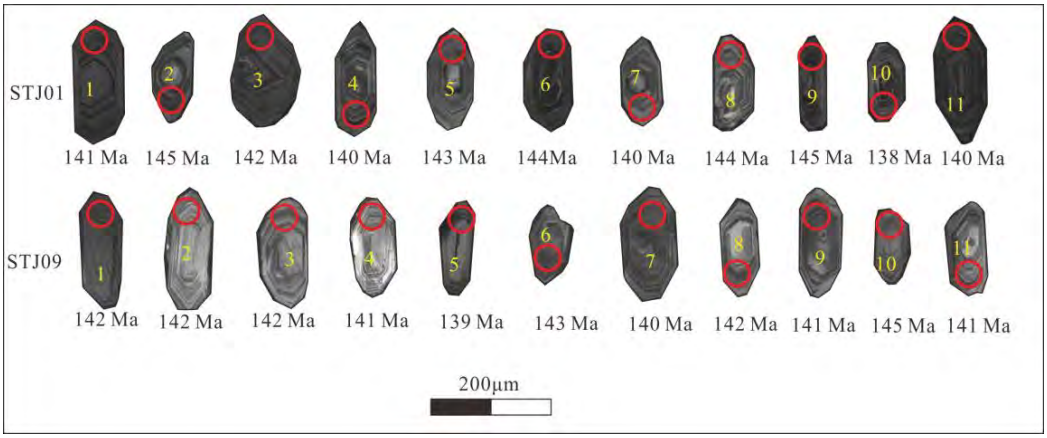

Figure 5

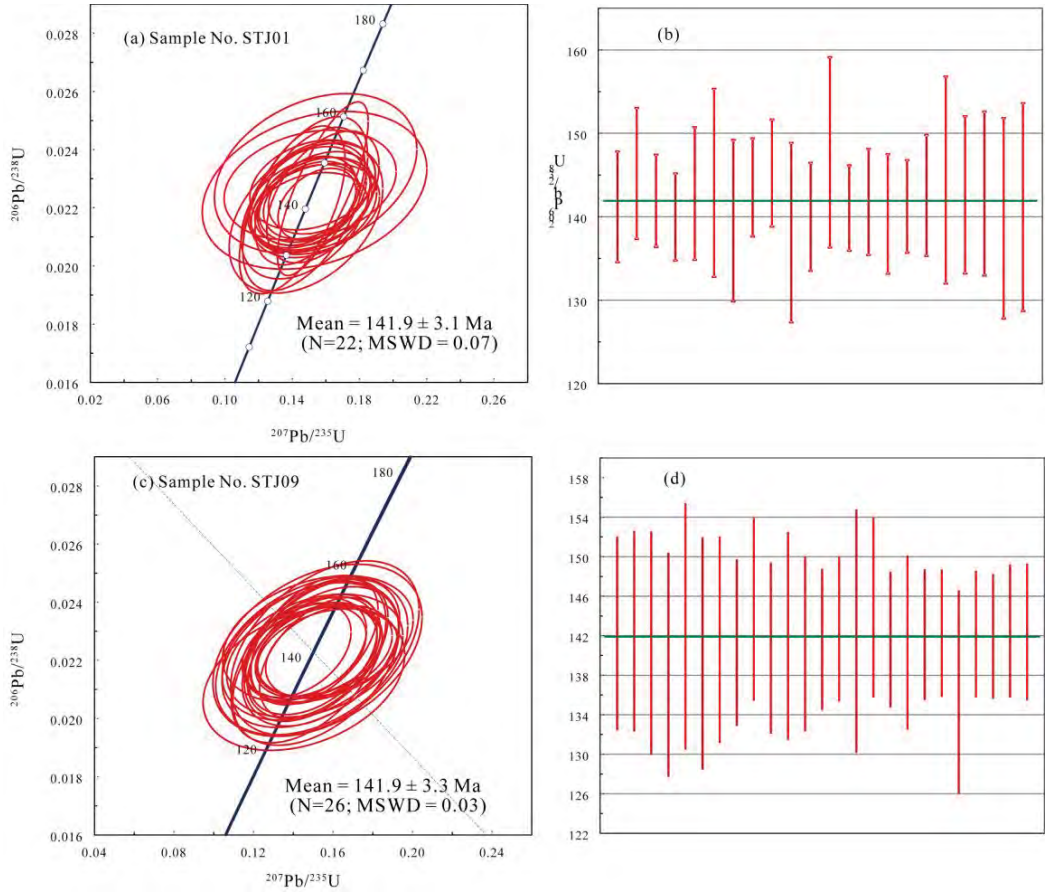

Figure 6

This is the peer-reviewed, final accepted version for American Mineralogist, published by the Mineralogical Society of America.
The published version is subject to change. Cite as Authors (Year) Title. American Mineralogist, in press.
DOI: https://doi.org/10.2138/am-2021-7871. http://www.minsocam.org/

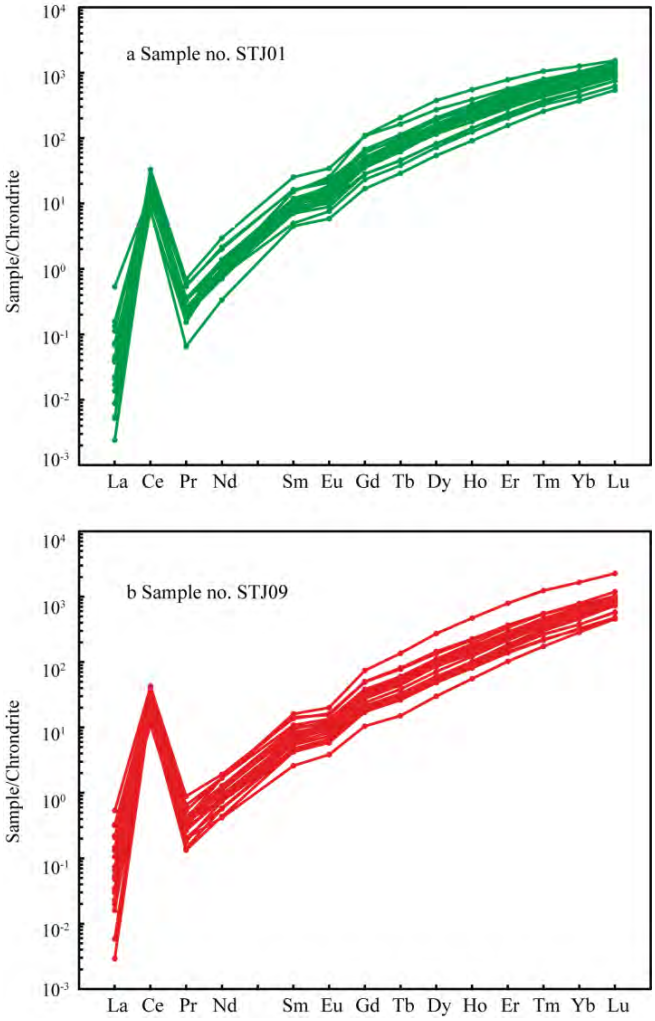

Figure 7

This is the peer-reviewed, final accepted version for American Mineralogist, published by the Mineralogical Society of America.
The published version is subject to change. Cite as Authors (Year) Title. American Mineralogist, in press.
DOI: https://doi.org/10.2138/am-2021-7871. http://www.minsocam.org/

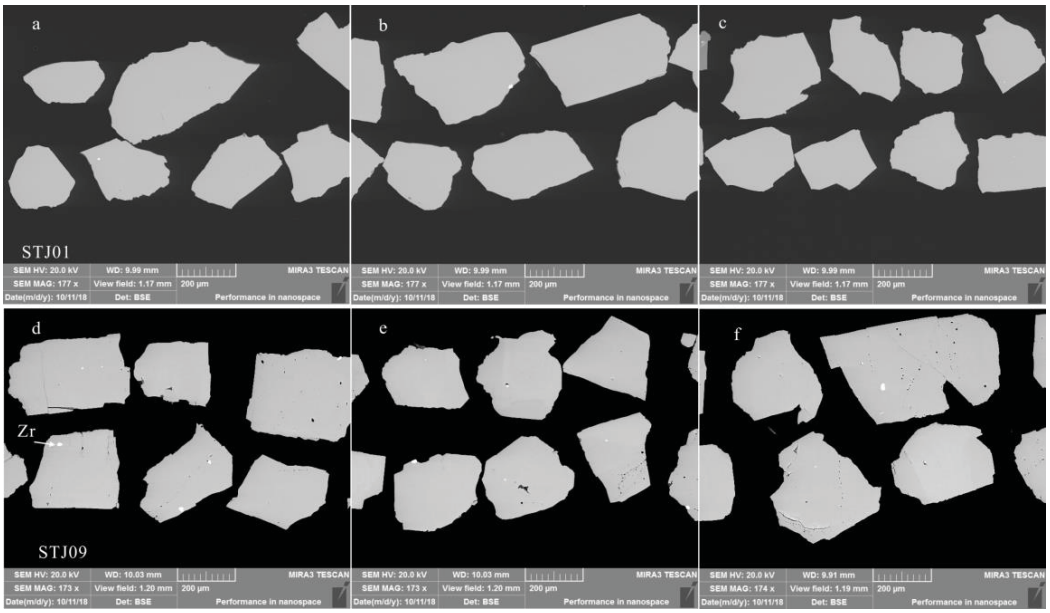

Figure 8

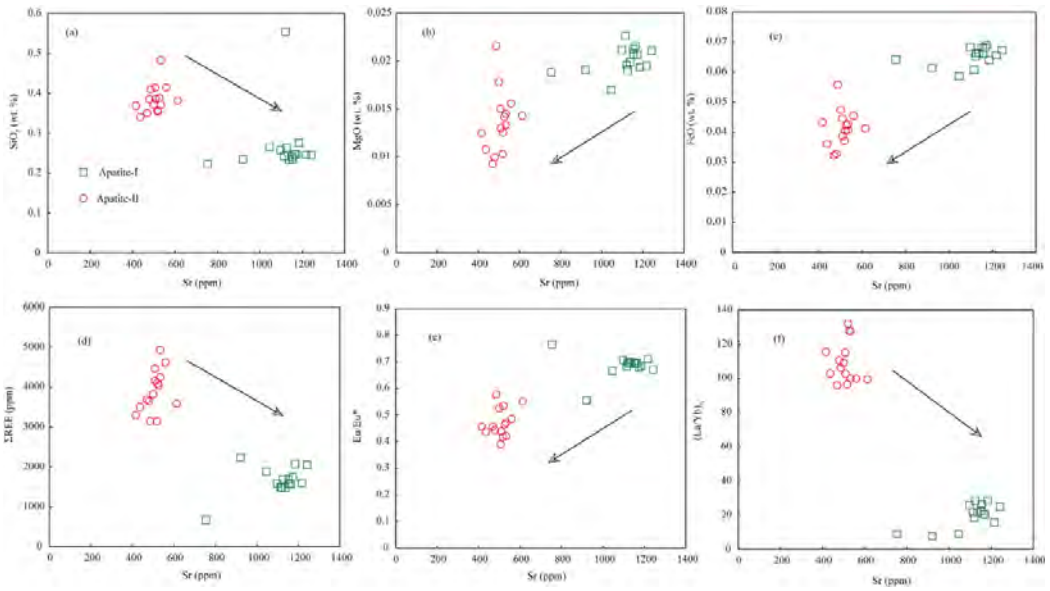

Figure 9

This is the peer-reviewed, final accepted version for American Mineralogist, published by the Mineralogical Society of America.
The published version is subject to change. Cite as Authors (Year) Title. American Mineralogist, in press.
DOI: https://doi.org/10.2138/am-2021-7871. http://www.minsocam.org/

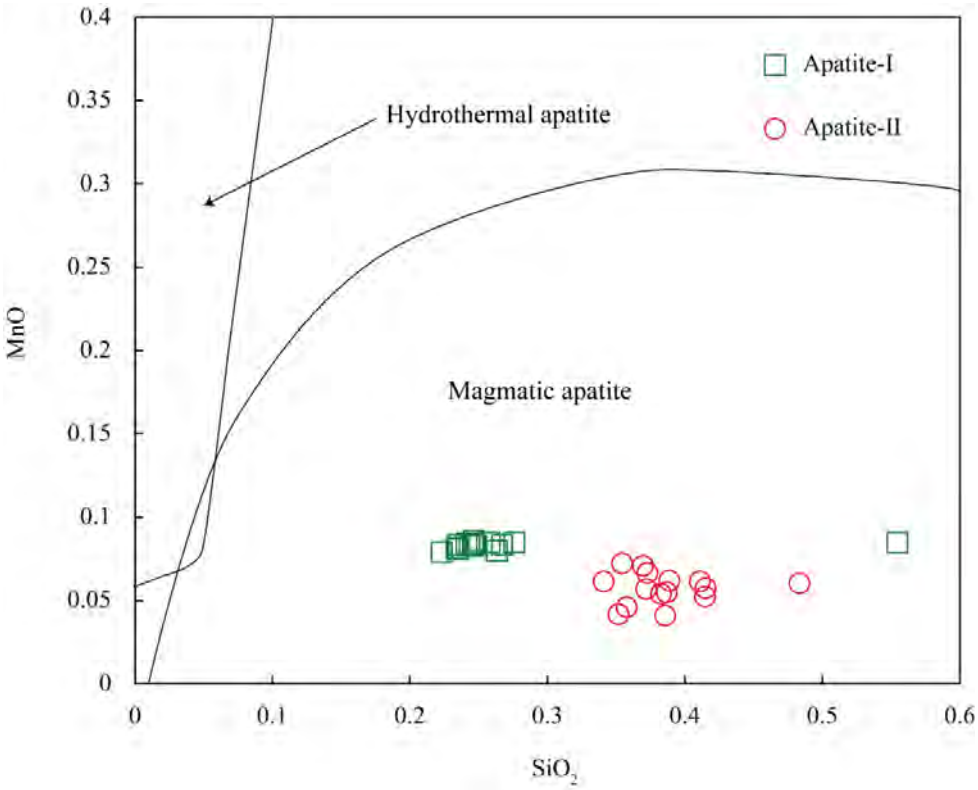

Figure 10

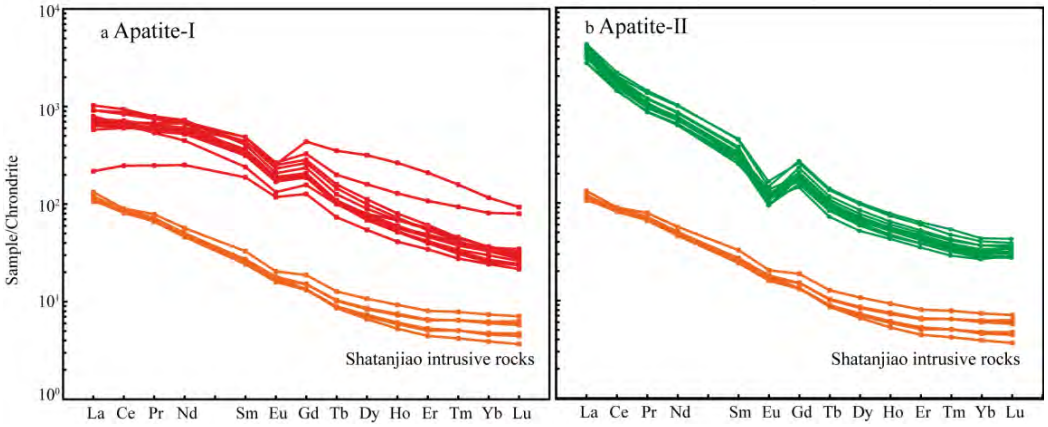

Figure 11

This is the peer-reviewed, final accepted version for American Mineralogist, published by the Mineralogical Society of America.
The published version is subject to change. Cite as Authors (Year) Title. American Mineralogist, in press.
DOI: https://doi.org/10.2138/am-2021-7871. http://www.minsocam.org/

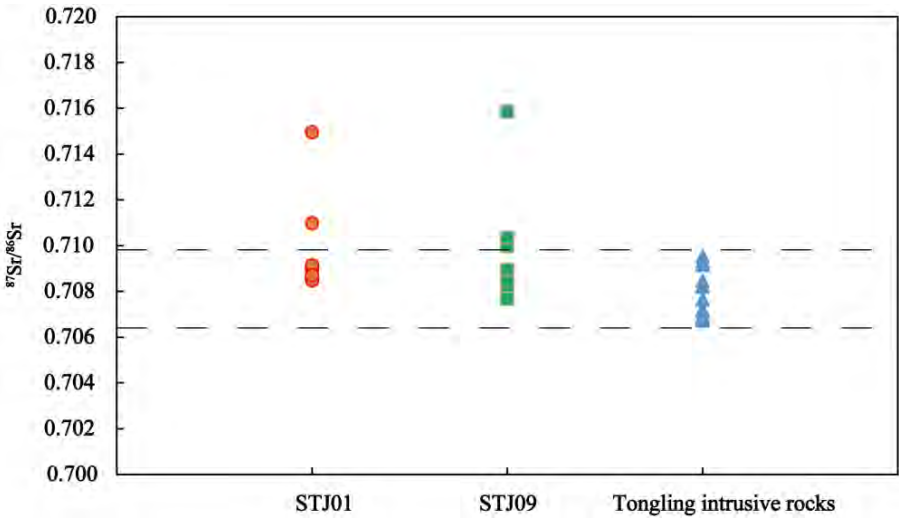

Figure 12

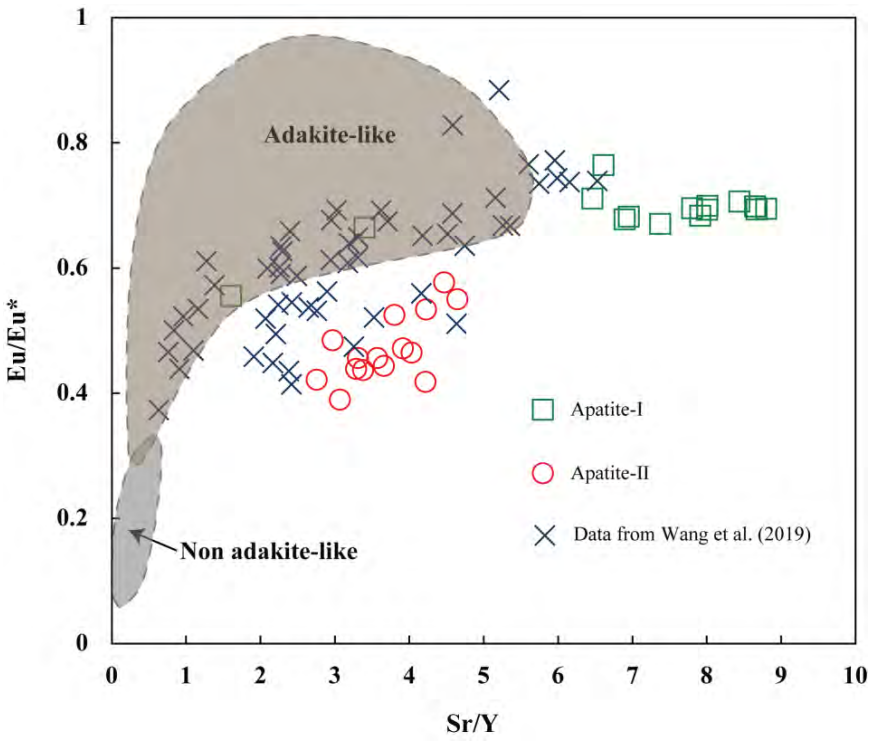

Figure 13

This is the peer-reviewed, final accepted version for American Mineralogist, published by the Mineralogical Society of America.
The published version is subject to change. Cite as Authors (Year) Title. American Mineralogist, in press.
DOI: https://doi.org/10.2138/am-2021-7871. http://www.minsocam.org/

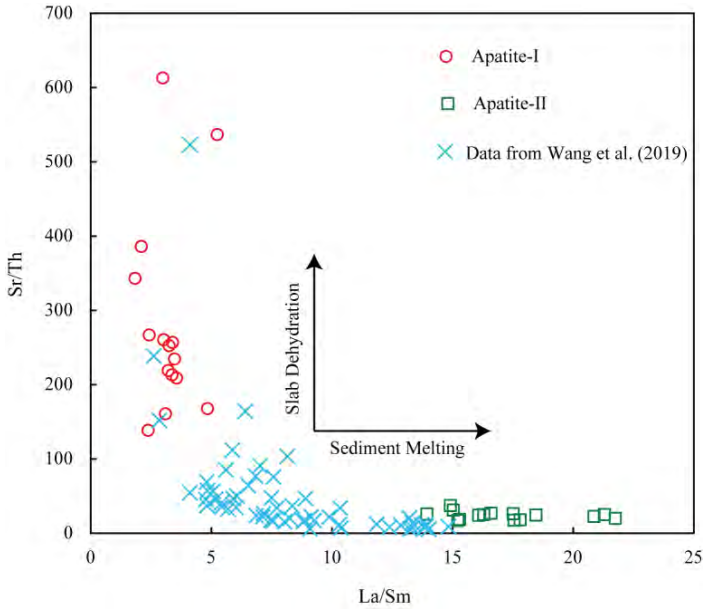

Figure 14

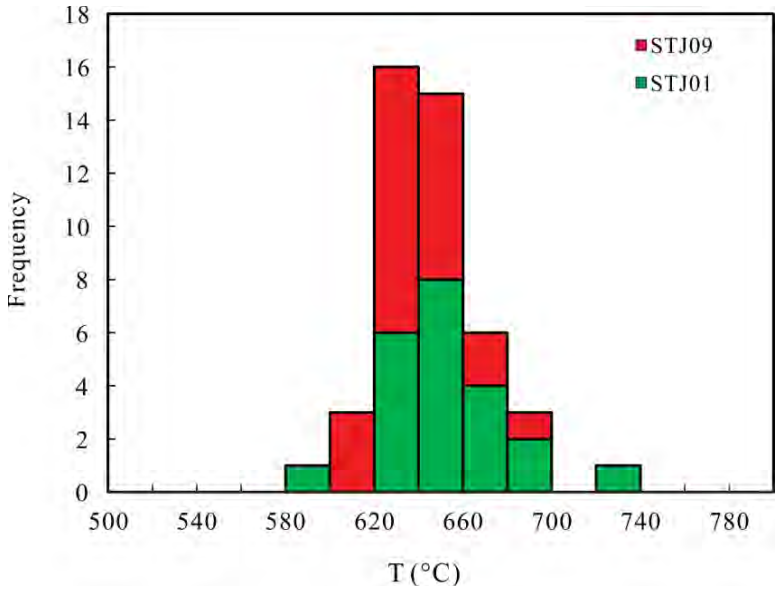

Figure 15

This is the peer-reviewed, final accepted version for American Mineralogist, published by the Mineralogical Society of America.
The published version is subject to change. Cite as Authors (Year) Title. American Mineralogist, in press.
DOI: https://doi.org/10.2138/am-2021-7871. http://www.minsocam.org/

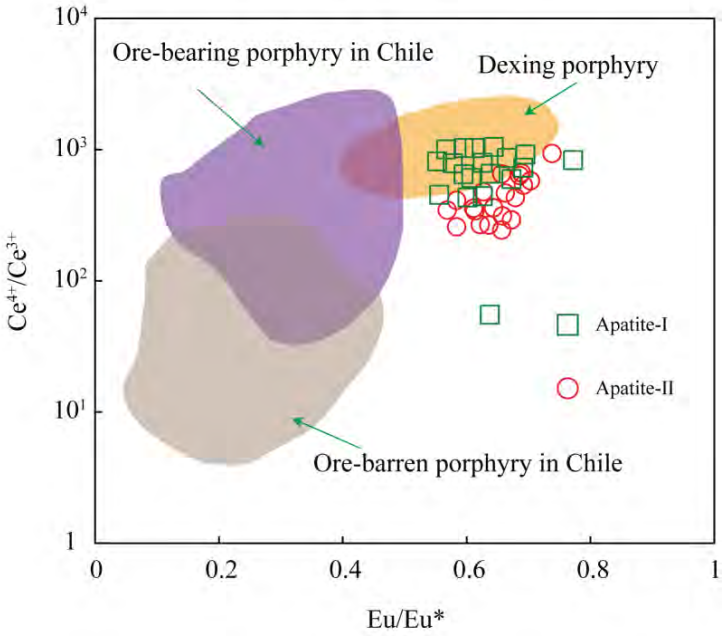

Figure 16